Technical Report No. 206

036040-3-T

COHERENT DEMODULATION OF THE IMPULSE RESPONSE OF BANDPASS FILTERS

by

D. Jaarsma

Approved by: Theodore G. Birdsall

Theodore G. Birdsall

for

COOLEY ELECTRONICS LABORATORY
Department of Electrical and Computer Engineering
The University of Michigan
Ann Arbor, Michigan

Contract No. N00014-67-A-0181-0032
Office of Naval Research
Department of the Navy
Arlington, Virginia 22217

August 1971

ABSTRACT

This report contains the analysis appropriate for the complex demodulation of the impulse response of realizable lumped-element filters. Plots of the time behavior of the log of the envelope, the instantaneous phase, and the instantaneous frequency, together with the conventional phase and amplitude of the transfer characteristic, are presented for a number of bandpass filters.

FOREWORD

In the signal processing of MIMI underwater acoustic propagation receptions, complex demodulation is used to determine the amplitude and phase of the complicated multipath arrivals. The interpretation of the amplitude as the envelope of a conventional pulse reception, and hence "path strength," is straightforward. The interpretation of the instantaneous phase as an indication of physical path structure is not so obvious. As an aid to the interpretation of phase, a number of examples of the complex demodulation of common classes of bandpass filters were analyzed, and the results plotted for comparison with physical measurements.

TABLE OF CONTENTS

LIST OF ILLUSTRATIONS

1. INTRODUCTION

In the study of underwater acoustic propagation, the multipath structure of the propagation is often studied using sharp impulsive sources, that is, explosions. The signal processing on reception consists normally of high-speed graphic recording of the reception. An alternative technique is to use high-power short pulses. This concentrates the transmission energy in the band of frequencies which one is most interested in. This latter is most appropriate in studying the difficulties that will arise in using a sonar system at this chosen carrier frequency. The usual signal processing upon reception is to envelope demodulate the reception; in conjunction with this high-speed graphic recording of the pulse, reception may be utilized to look at the fine detailed structure in the carrier. Perhaps additional processing in terms of spectrographs will be used to study dispersion of the pulse caused by the propagation.

In the propagation studies of Project MIMI the medium has been shown to be very complicated, but yet phase stable. This means that there is a possibility of extremely high gains in signal processing possible if suitable transmissions are used. The actual transmissions used in Project MIMI are pseudo-random coded transmissions. The reception technique converts these back to the equivalent pulse

at much higher power, utilizes extremely narrow comb filters to reject surface reverberation, and then coherently demodulates the result so that the fine detail structure of the reception, as well as the envelope, is available. Both the envelope function and the phase function are displayed. This has two basic advantages. First, the stability in phase allows the comparison of repeated receptions, and the determination of very weak receptions by noting the stability in received phase; in the absence of received energy the indicated phase is uniformly distributed over all possible angles, and quite recognizable from a weak arrival which yields a concentrated or nearly repeated phase. Secondly, the instantaneous frequency of the arrival can be measured as a function of delay from the main arrival, by differentiating the phase function. The equations for the processed pulse reception are usually written in the form of Eq. 1.

$$\left.\begin{aligned} h(\tau) &= R(\tau)\cos\left[\omega_0\tau + \theta(\tau)\right] \\ f_i(\tau) &= \omega_0 + d\theta/d\tau \end{aligned}\right\} \qquad (1)$$

where

$R(\tau)$ is the envelope of the reception,

ω_0 is the carrier frequency, and

$\theta(t)$ is the relative phase shift of the received waveform compared to a stable reference at the carrier frequency,

$f_i(\tau)$ is the instantaneous frequency of the reception.

The actual demodulation process used in Project MIMI is referred to as "phase coherent demodulation," and is generally known in recent years as "complex demodulation." For the actual processing it is more appropriate to write the received waveform of Eq. 1 in Cartesian coordinates.

$$h(\tau) = x(\tau) \cos \omega_0 \tau - y(\tau) \sin \omega_0 \tau \qquad (2)$$

The relationship between the envelope and phase functions, and these processing coordinates is shown in Fig. 1.

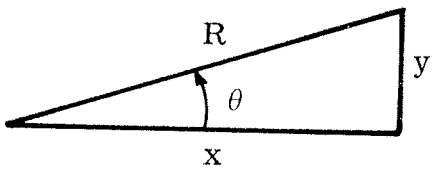

$$x(\tau) = R(\tau) \cos \theta(\tau)$$

$$y(\tau) = R(\tau) \sin \theta(\tau)$$

Fig. 1. Cartesian vs. polar coordinates

This relationship is the usual triangular relationship between magnitude and phase on the one hand and orthogonal components on the other. This type of demodulation has earned the nickname "complex demodulation" because one may write the reception in terms of a complex quantity by imagining that $x(\tau)$ is the real part and $y(\tau)$ the imaginary part, or if one chooses, that $R(\tau)$ is the magnitude and $\theta(\tau)$ is the phase.

$$z(\tau) = x(\tau) + j\, y(T) = R(\tau)\, e^{j\theta(\tau)} \qquad (3)$$

This is merely a compact form of writing the coordinate systems shown in Fig. 1.

Using the complex form shown in Eq. 3 the received and demodulated pulse response shown in Eq. 1 can be written as the real part of a complex number

$$h(\tau) = \mathrm{Re}\left[z(\tau)\, e^{j\omega_0 \tau}\right] \qquad (4)$$

Although this may seem a little artificial, it displays to the analyst that the actual reception is simply formed by complex demodulation and then shifted in frequency back around the carrier frequency ω_0.

Complex demodulation and display of the envelope and phase functions has proved to be an extremely useful signal processing technique. Figure 2 shows a typical overlay of ten such demodulations taken by Project MIMI on a 43-mile transmission. The upper graph is the envelope, the lower graph displays the demodulated phase as a function of time. From the repeatability of the phase diagram one can see immediately that the arrivals are quite phase coherent, that the instantaneous frequency shifts throughout the duration of the reception, and that one may determine the presence of very weak paths in the tail or later arrivals of the reception by noting the repeatability of the phase, even though the magnitude is quite small.

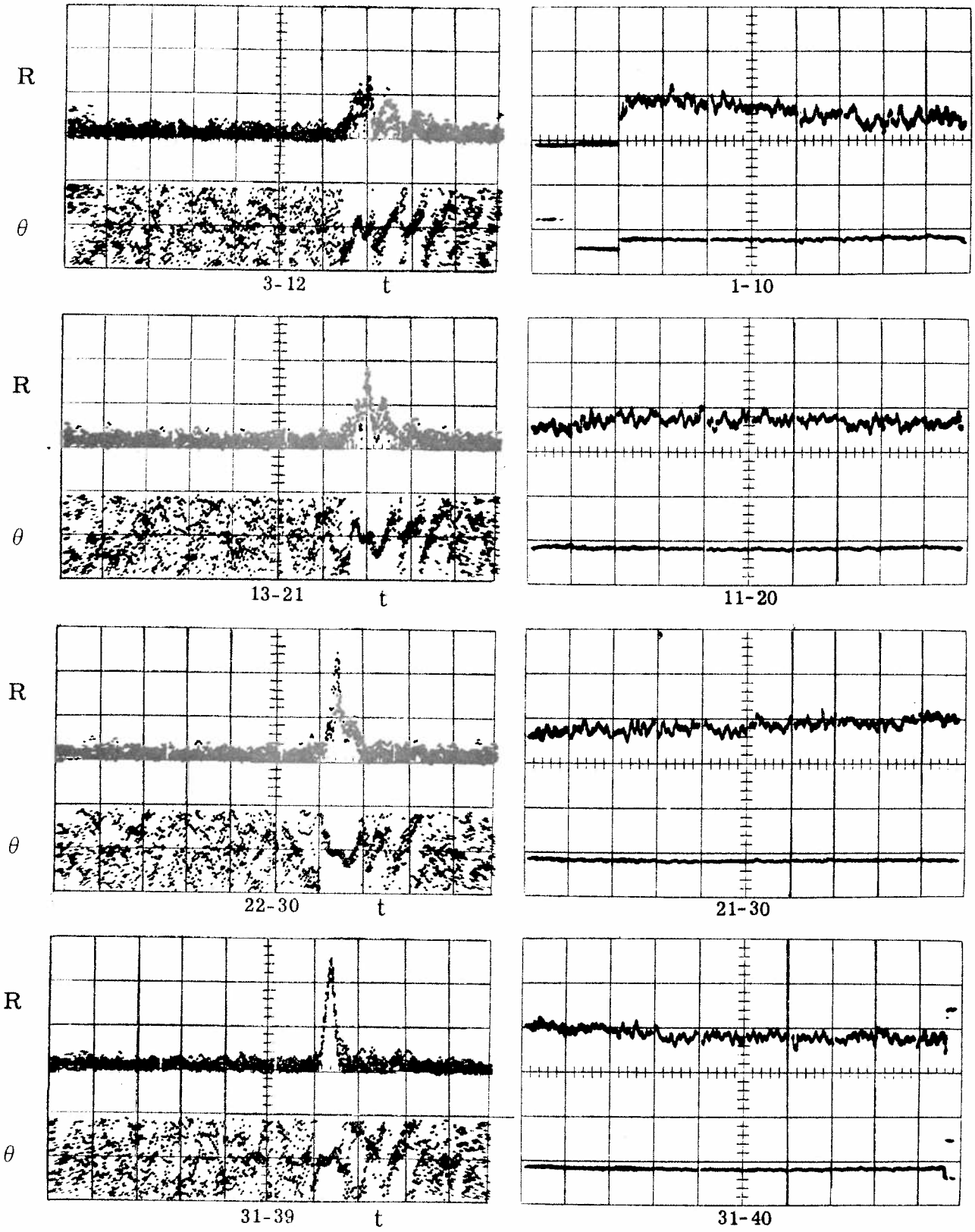

SEQ, R = 0.5 V/div
t = 120 msec/div

CW, R = 0.2 V/div
t = 120 msec/div

Fig. 2. AMSEQ 11 August 1966 1445 - 1457 hours

Very little theory is available to guide one in using such a detailed picture to infer the properties of the medium. The present study was undertaken in order to gain some insight into the meaning of the analysis, and in particular in the behavior of the phase function when the amplitude is very low. Specifically the medium was modeled as a bandpass filter of any one of many classical types familiar to electrical engineers. The impulse response of the chosen filter was then coherently demodulated, and the envelope and phase functions of this impulse response displayed similar to the displays used in the Project MIMI propagation studies. This report contains the derivation of the technique for coherently demodulating the impulse response of a realizable filter, and displays many of these graphs so that they may be used as a basis for comparing actual receptions of underwater acoustic signals.

2. THE COHERENT DEMODULATION OF A BANDPASS IMPULSE RESPONSE

Some classical low-pass filters are reviewed in Appendix A. A technique for converting from bandpass to low-pass is discussed in Appendix B, and it is shown that the transfer function of a bandpass filter which has no repeated poles can be written in its partial fraction expansion as

$$H(s) = \sum_{i=1}^{n} \frac{r_i}{s - s_i} + \frac{r_i^*}{s - s_i^*} \tag{5}$$

The summation has been written in two parts where the poles, s_i, that occur in the upper left quadrant have been singled out. The poles in the lower left quadrant are the complex conjugates of those in the upper left quadrant, and it is assumed that all of the poles are in the left half plane; that is, we are studying a stable realizable bandpass filter. The * denotes complex conjugate, and the real and imaginary parts of the pole are denoted by

$$s_i = \sigma_i + j\omega_i , \qquad \sigma_i < 0, \quad \omega_i > 0 \tag{6}$$

For simplicity of complex demodulation, the complex impulse response due to just the upper half plane poles will be utilized.

$$h_u(\tau) = \sum_{i=1}^{n} r_i e^{s_i \tau} u(\tau) \tag{7}$$

where

$u(\tau)$ is the unit step function.

The total impulse response of the filter is the sum of the contributions from both upper and lower half planes and is

$$h(\tau) = h_u(\tau) + h_u^*(\tau) = 2\,\mathrm{Re}[h_u(\tau)] \tag{8}$$

Comparing Eq. 8 and Eq. 4 one determines immediately

$$z(\tau)\, e^{j\omega_0 \tau} = 2\, h_u(\tau) \tag{9}$$

This is why the complex response from the upper half plane poles only was singled out. Shifting the exponential term to the other side of the equation, we have

$$z(\tau) = 2\, h_u(\tau)\, e^{-j\omega_0 \tau} = 2 \sum_{i=1}^{n} r_i e^{p_i \tau} u(\tau) \tag{10}$$

where

$$p_i = s_i - j\omega_0 = \sigma_i + j(\omega_i - \omega_0) \tag{11}$$

This shows that $z(\tau)$ is the response due to poles at new positions shifted from their bandpass location down to near the origin with the

residues r_i the same as for the bandpass function. Complex demodulation can be obtained by writing Eq. 10 in Cartesian coordinates

$$z(\tau) = x(\tau) + j\, y(\tau) = 2 \sum_{i=1}^{n} r_i e^{p_i \tau} u(\tau) \tag{12}$$

and using the computer to evaluate the real and imaginary parts of this complex summation. The instantaneous frequency as defined in Eq. 1 can be determined from the Cartesian coordinates, and the use of the coordinate change shown in Fig. 1.

$$\begin{aligned} f_i(\tau) &= \omega_0 + \frac{d\theta(\tau)}{d\tau} \\ &= \omega_0 + \frac{x(\tau)\,\dot{y}(\tau) - \dot{x}(\tau)\,y(\tau)}{x^2(\tau) + y^2(\tau)}, \qquad \tau > 0 \end{aligned} \tag{13}$$

The derivatives of the complex demodulation are determined by differentiating Eq. 12

$$\dot{z}(\tau) = \dot{x}(\tau) + j\,\dot{y}(\tau) = 2 \sum_{i=1}^{n} r_i p_i e^{p_i \tau}, \qquad \tau > 0 \tag{14}$$

and again using the computer to evaluate the real and imaginary parts of this complex summation.

3. DISPLAY OF THE COMPLEX DEMODULATION FOR VARIOUS TYPICAL BANDPASS FILTERS

Figures 3-5 show the results of complex demodulation for various Butterworth filters. Figures 6-8 show the same results for various Chebyshev filters. The figures on the left side show the time domain representation of the impulse response while the figures on the right side show the frequency domain representation. Figure 9 shows the time domain representation of the magnitude function R on a linear scale. The bandwidth of each of the filters of Figs. 3-8 is 100 Hz with a center frequency of 420 Hz. The parameter n refers to the order of the filter while the parameter ϵ is the ripple factor for the Chebyshev filter.

The dominant feature that shows up on all of the figures is the sweeping phase for fairly low amplitude levels. The same sweeping phase appears in MIMI data of Fig. 2. At these low amplitude levels the nth order filter behaves as if it were a first order filter with the dominant effect due to the pole nearest the imaginary axis. The conclusion to be drawn from this comparison is that the MIMI channel appears to behave as a first order bandpass filter for low level signals.

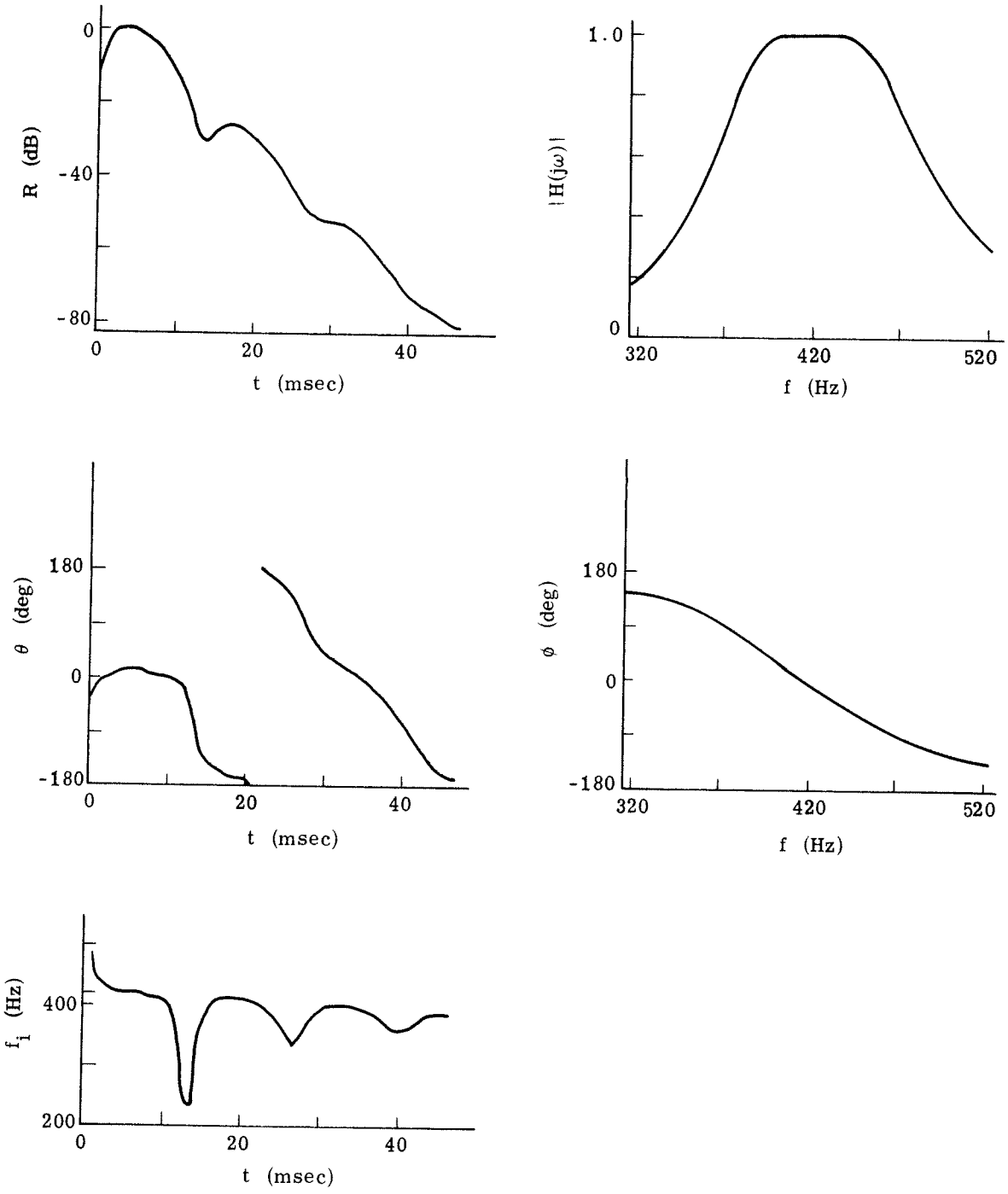

Fig. 3. Time and frequency domain representation of the impulse response of a Butterworth bandpass filter, n = 2

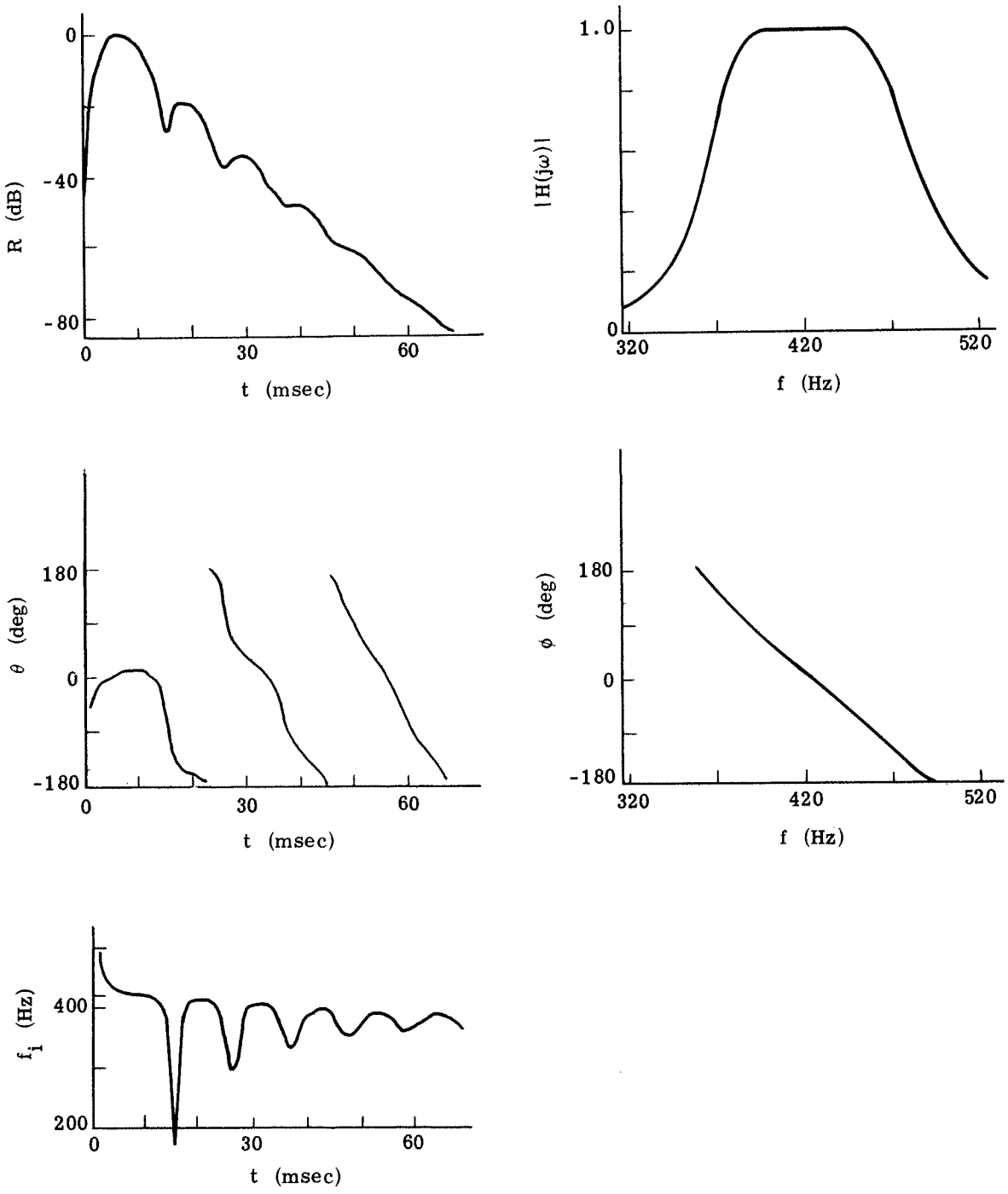

Fig. 4. Time and frequency domain representation of the impulse response of a Butterworth bandpass filter, n = 3

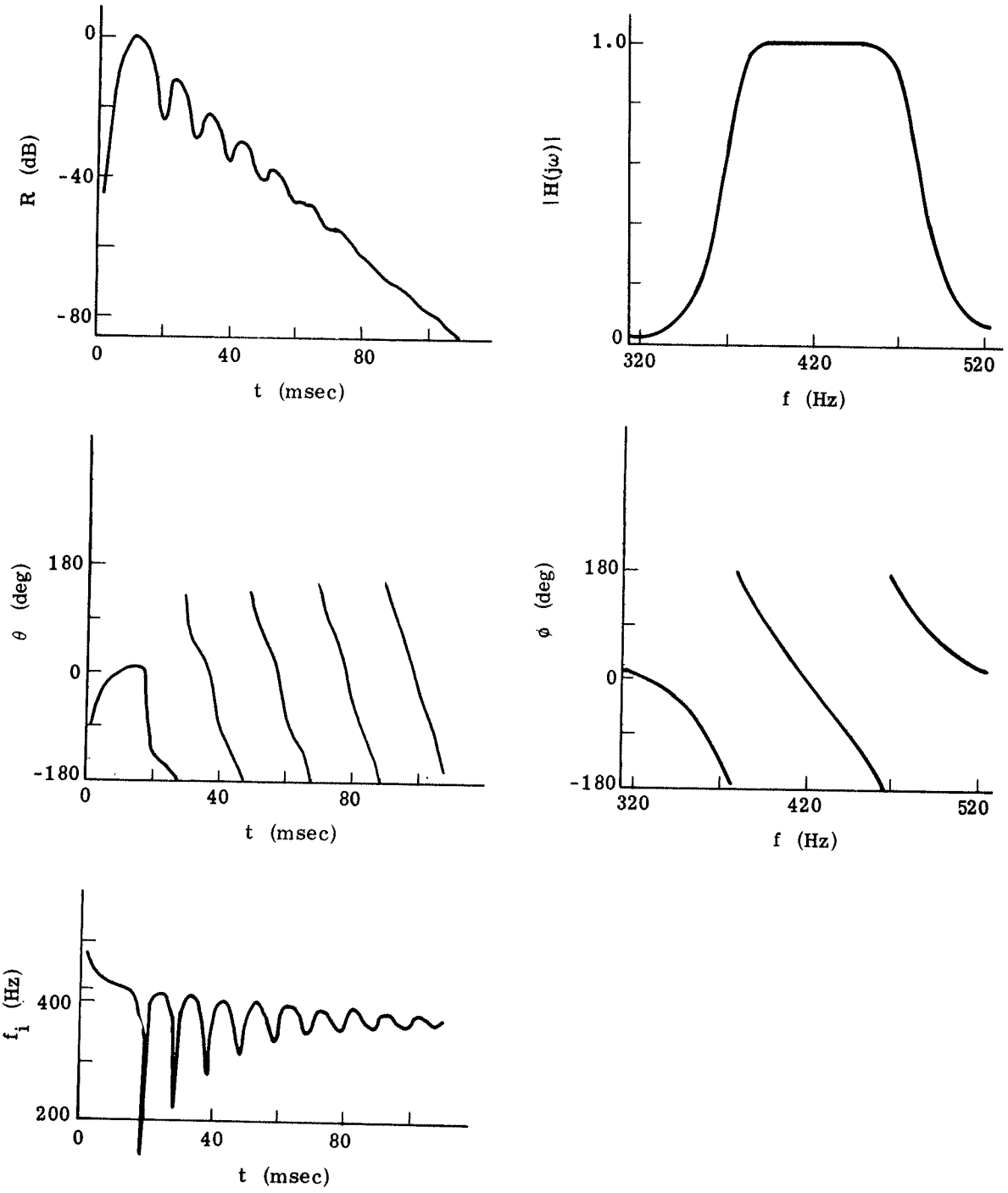

Fig. 5. Time and frequency domain representation of the impulse response of a Butterworth bandpass filter, n = 5

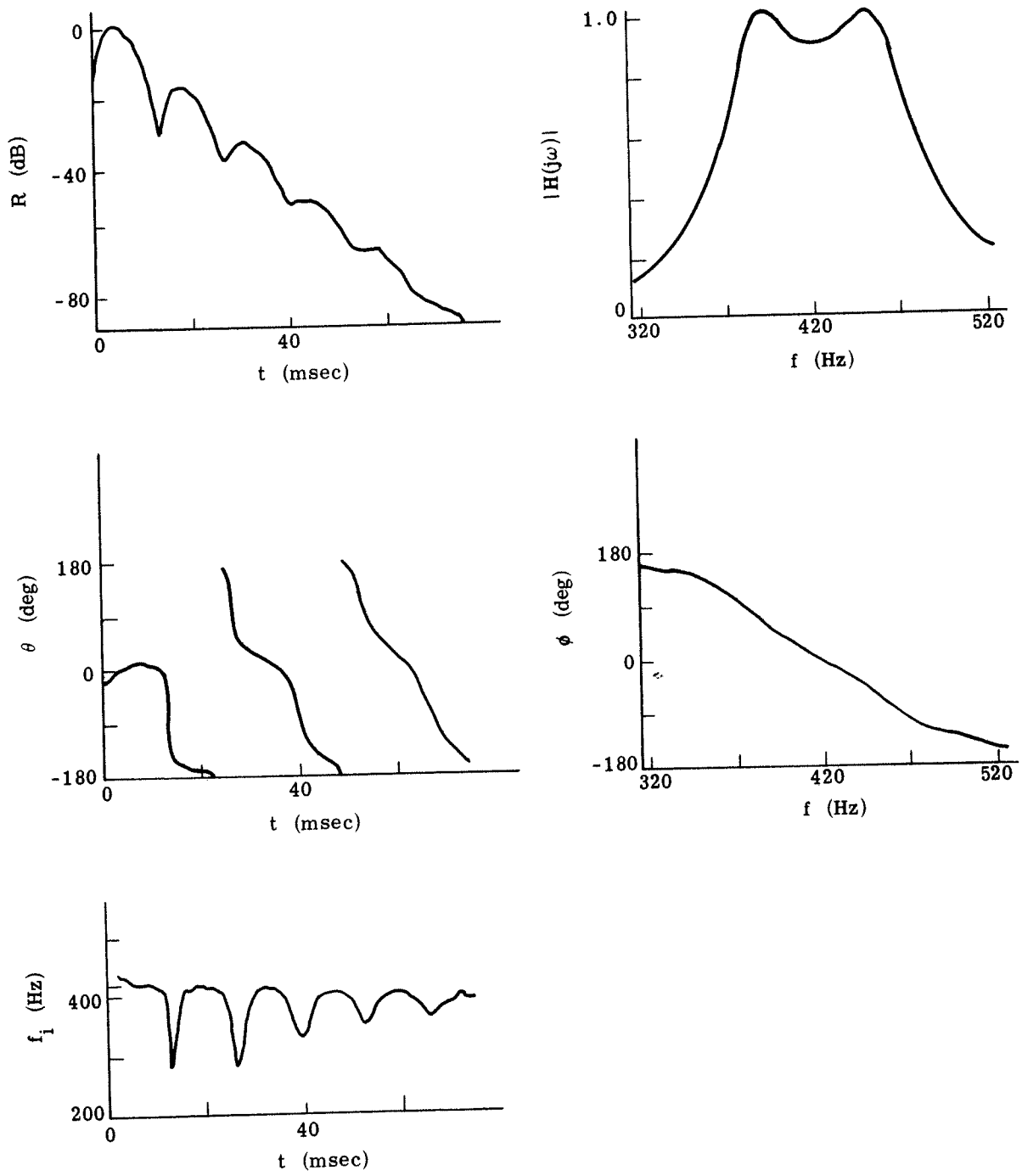

Fig. 6. Time and frequency domain representation of the impulse response of a Chebyshev bandpass filter, n = 2, ϵ = .5

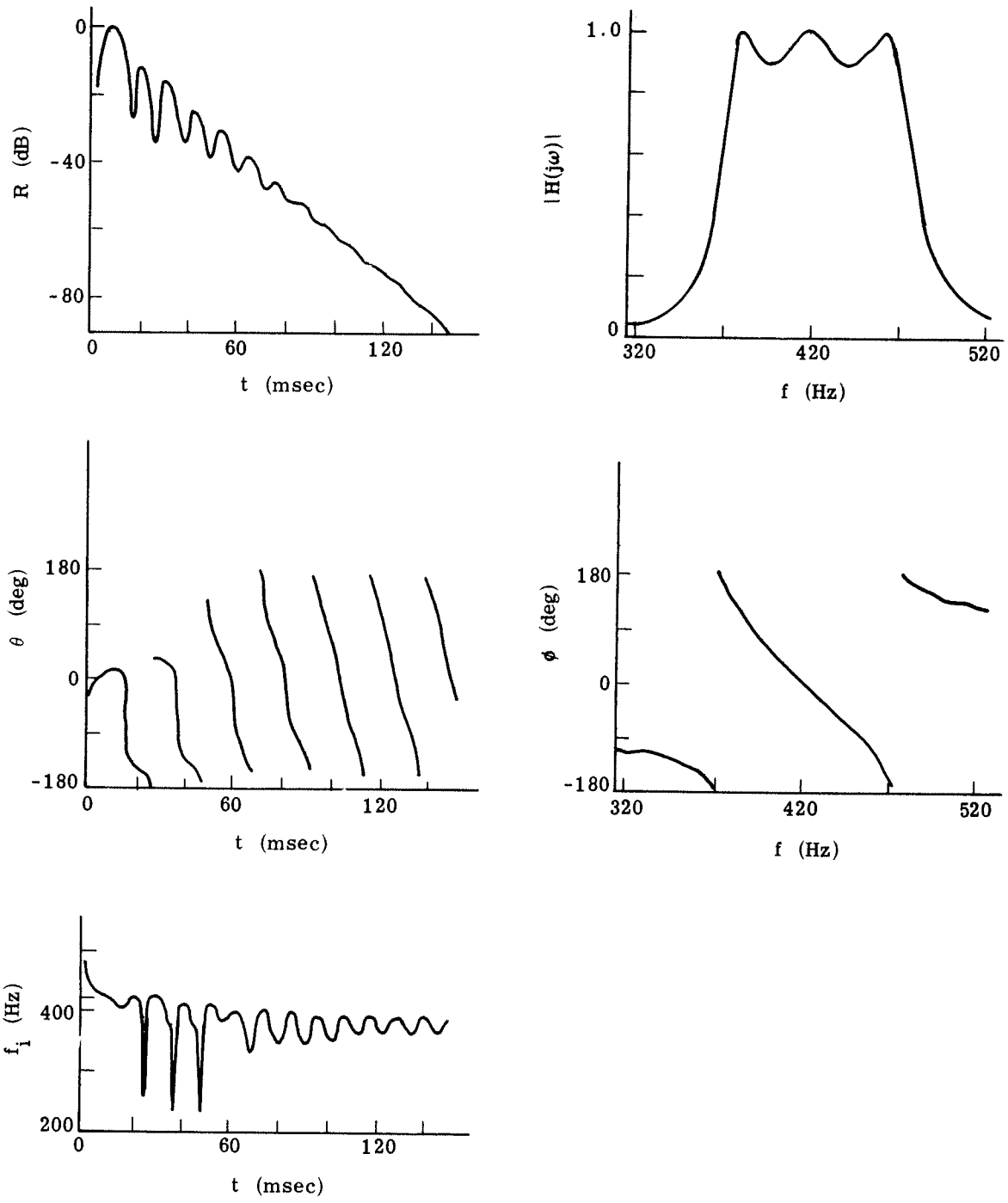

Fig. 7. Time and frequency domain representation of the impulse response of a Chebyshev bandpass filter, n = 3, ϵ = .5

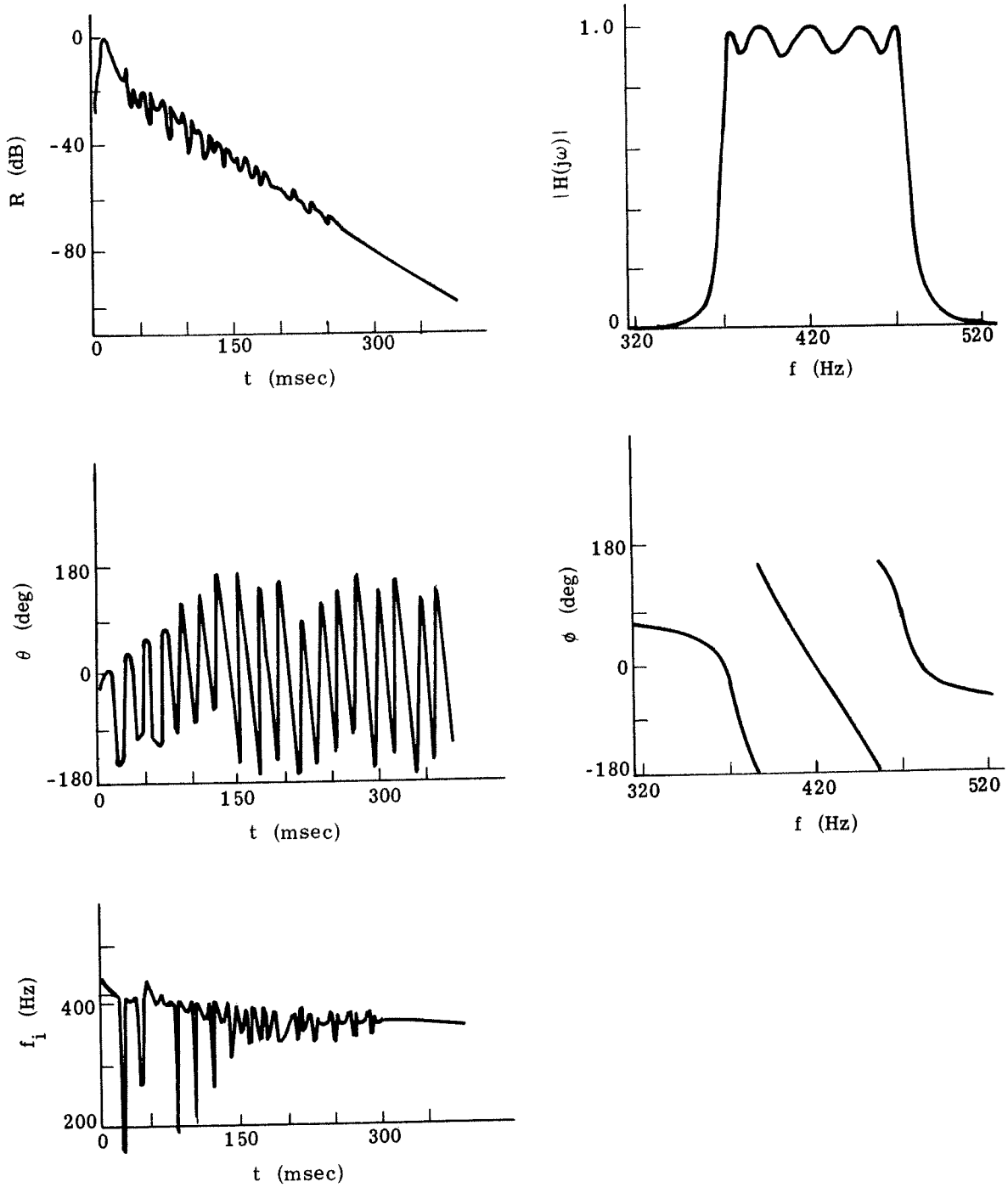

Fig. 8. Time and frequency domain representation of the impulse response of a Chebyshev bandpass filter, n = 5, ϵ = .5

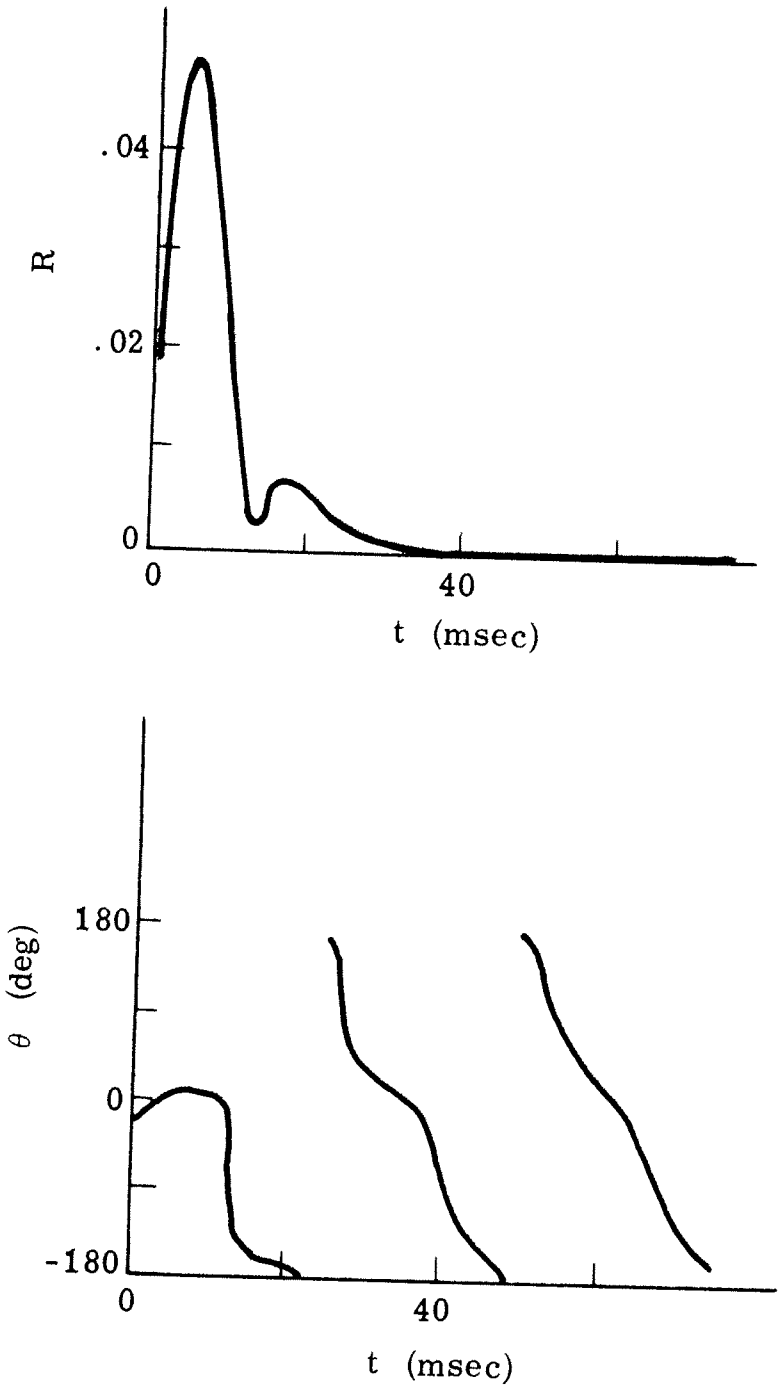

Fig. 9. Demodulated time response of the impulse response of a Chebyshev bandpass filter, n = 2, ϵ = .5

APPENDIX A

CLASSICAL LOW-PASS FILTERS

The Butterworth and the Chebyshev filters were considered as appropriate representations of low-pass filters. For convenience, the center frequency was normalized to $\omega_0 = 1$.

1) Butterworth filter of nth order--maximally flat magnitude function

$$|H_n(j\omega)| = \frac{1}{\left(1 + \omega^{2n}\right)^{\frac{1}{2}}}$$

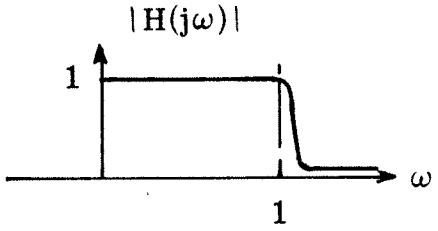

and

$$H_n(s) = \frac{1}{\prod_{i=1}^{n} (s - s_i)}$$

where

$$s_i = \sigma_i + j\omega_i$$

and

$$\sigma_i = \sin\left(\frac{2i-1}{n} \cdot \frac{\pi}{2}\right)$$

$$i = 1, 2, \ldots, n$$

$$\omega_i = \cos\left(\frac{2i-1}{n} \cdot \frac{\pi}{2}\right)$$

$$i = 1, 2, \ldots, n$$

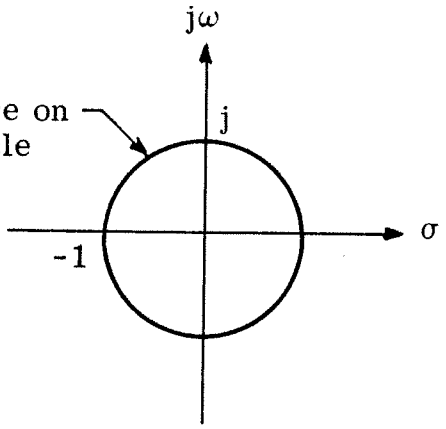

2) Chebyshev filter of nth order--equal-ripple magnitude function

$$|H_n(j\omega)| = \frac{1}{1 + \epsilon^2 C_n^2(\omega)}$$

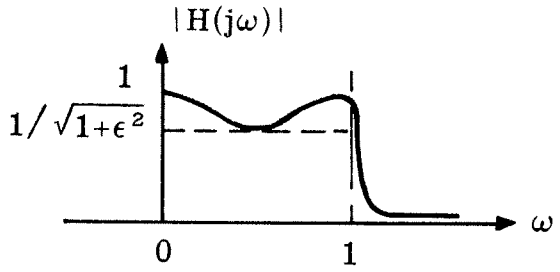

and

$$H_n(s) = \frac{1}{\prod_{i=1}^{n} (s - s_i)}$$

where

$$s_i = \sigma_i + j\omega_i \qquad i = 1, 2, \ldots, n$$

and

$$\sigma_i = \sin\left(\frac{2i-1}{n} \cdot \frac{\pi}{2}\right) \tanh(v)$$

$$\omega_i = \cos\left(\frac{2i-1}{n} \cdot \frac{\pi}{2}\right)$$

$$v = \frac{1}{n} \sinh^{-1}\left(\frac{1}{\epsilon}\right)$$

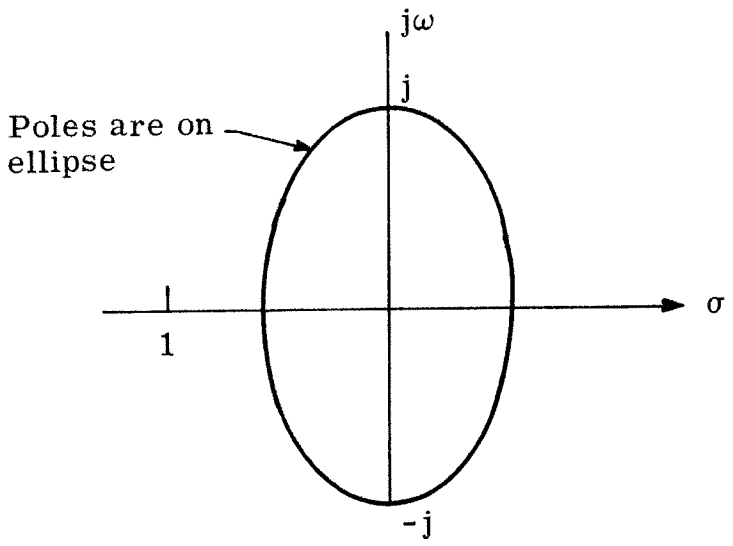

$C_n(\omega)$ is the nth order Chebyshev polynomial

$$C_n(\omega) = \begin{cases} \cos[n \cos^{-1}(\omega)] & 0 \leq \omega \leq 1 \\ \cosh[n \cosh^{-1}(\omega)] & \omega > 1 \end{cases}$$

with

$$C_0(\omega) = 1$$

$$C_1(\omega) = \omega$$

$$\vdots$$

$$C_{k+1}(\omega) = 2\omega\, C_k(\omega) - C_{k-1}(\omega)$$

APPENDIX B

CONVERSION FROM LOW-PASS TO BANDPASS

Let $L(z)$ be a low-pass transfer function of nth order. Assume only single order poles are present. Denote the poles by z_i and the residues by p_i. Hence

$$L(z) = \sum_{i=1}^{n} \frac{p_i}{z - z_i}$$

If $L(z)$ is positive real (the network is stable), then complex poles occur in conjugate pairs and their residues are conjugates. If the poles are in the vicinity of the origin with $|z_i| < 1$, $i = 1, 2, \ldots, n$, then the normalized transformation

$$z = s + \frac{1}{s}$$

is used to convert from the low-pass transfer function $L(z)$ to the bandpass transfer function

$$H(s) \triangleq L(s + \frac{1}{s})$$

$$= \sum_{i=1}^{n} \frac{t_i}{s - s_i} + \frac{t_i'}{s - s_i'}$$

where

$$s_i = .5z_i + \sqrt{.25z_i^2 - 1} \quad [1]$$

$$s_i' = .5z_i - \sqrt{.25z_i^2 - 1}$$

$$t_i = \frac{p_i s_i}{s_i - s_i'}$$

$$t_i' = -\frac{p_i s_i'}{s_i - s_i'}$$

Some Observations

1) Each pole z_i (in the vicinity of the origin) is mapped into an UHP pole s_i (close to j) and a LHP pole s_i' (close to $-j$) with $|s_i - j| \simeq |s_i' + j| \simeq 2|z_i|$, $i = 1, 2, \ldots, n$.

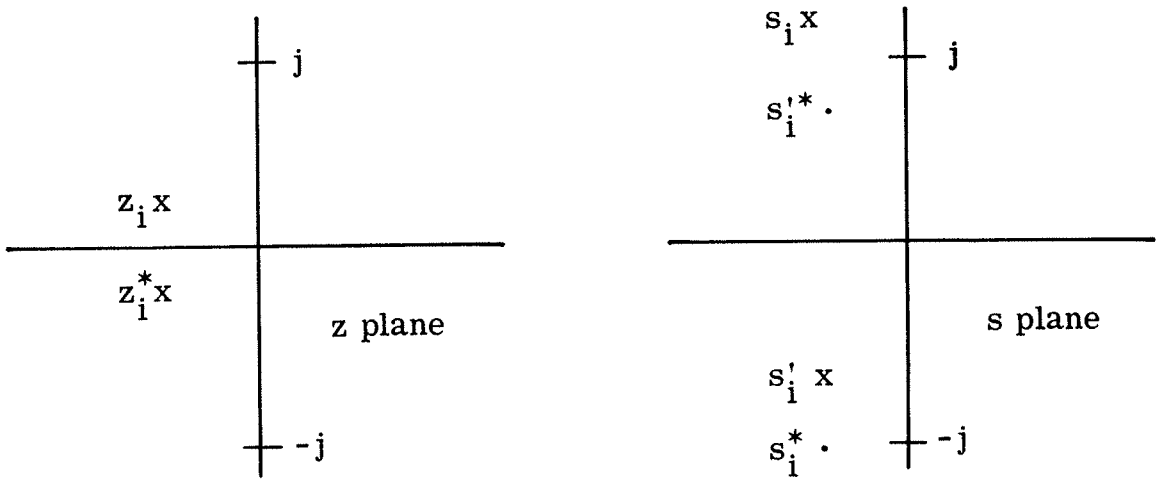

Pole Locations

---

[1] In terms of Cartesian coordinates

$$\sqrt{x+jy} = \sqrt{\frac{\sqrt{x^2+y^2}+x}{2}} + j\,\mathrm{sgn}(y)\sqrt{\frac{\sqrt{x^2+y^2}-x}{2}}$$

where

$$\mathrm{sgn}(y) = \begin{cases} 1 & y \geq 0 \\ -1 & y < 0 \end{cases}$$

2) Symmetry considerations enable one to write H(s) as a sum of UHP poles and LHP poles, i.e.,

$$H(s) = \sum_{i=1}^{n} \frac{\beta_i}{s - \alpha_i} + \frac{\beta_i^*}{s - \alpha_i^*}$$

where

$$\alpha_i = \begin{cases} s_i & \text{Im } s_i > 0 \\ s_i^* & \text{Im } s_i < 0 \end{cases}$$

$$\beta_i = \begin{cases} t_i & \text{Im } s_i > 0 \\ t_i^* & \text{Im } s_i < 0 \end{cases}$$

DISTRIBUTION LIST

	No. of Copies
Office of Naval Research (Code 468) (Code 102-OS) (Code 480) Navy Department Washington, D. C. 20360	1 1 1
Director, Naval Research Laboratory Technical Information Division Washington, D. C. 20390	6
Director Office of Naval Research Branch Office 1030 East Green Street Pasadena, California 91101	1
Office of Naval Research San Francisco Area Office 1076 Mission Street San Francisco, California 94103	1
Director Office of Naval Research Bramch Office 495 Summer Street Boston, Massachusetts 02210	1
Office of Naval Research New York Area Office 207 West 24th Street New York, New York 10011	1
Director Office of Naval Research Branch Office 219 South Dearborn Street Chicago, Illinois 60604	1
Commanding Officer Office of Naval Research Branch Office Box 38 FPO New York 09510	8

DISTRIBUTION LIST (Cont.)

	No. of Copies
Commander Naval Ordnance Laboratory Acoustics Division White Oak, Silver Spring, Maryland 20907 Attn: Dr. Zaka Slawsky	1
Commanding Officer Naval Ship Research & Development Center Annapolis, Maryland 21401	1
Commander Naval Undersea Research & Development Center San Diego, California 92132 Attn: Dr. Dan Andrews Mr. Henry Aurand	2
Chief Scientist Navy Underwater Sound Reference Division P. O. Box 8337 Orlando, Florida 32800	1
Commanding Officer and Director Navy Underwater Systems Center Fort Trumbull New London, Connecticut 06321	1
Commander Naval Air Development Center Johnsville, Warminster, Pennsylvania 18974	1
Commanding Officer and Director Naval Ship Research and Development Center Washington, D. C. 20007	1
Superintendent Naval Postgraduate School Monterey, California 93940	1
Commanding Officer & Director Naval Ship Research & Development Center* Panama City, Florida 32402	1

*Formerly Mine Defense Lab.

DISTRIBUTION LIST (Cont.)

	No. of Copies
Naval Underwater Weapons Research & Engineering Station Newport, Rhode Island 02840	1
Superintendent Naval Academy Annapolis, Maryland 21401	1
Scientific and Technical Information Center 4301 Suitland Road Washington, D. C. 20390 Attn: Dr. T. Williams Mr. E. Bissett	2
Commander Naval Ordnance Systems Command Code ORD-03C Navy Department Washington, D. C. 20360	1
Commander Naval Ship Systems Command Code SHIPS 037 Navy Department Washington, D. C. 20360	1
Commander Naval Ship Systems Command Code SHIPS 00V1 Washington, D. C. 20360 Attn: CDR Bruce Gilchrist Mr. Carey D. Smith	2
Commander Naval Undersea Research & Development Center 3202 E. Foothill Boulevard Pasadena, California 91107	1
Commanding Officer Fleet Numerical Weather Facility Monterey, California 93940	1

DISTRIBUTION LIST (Cont.)

	No. of Copies
Defense Documentation Center Cameron Station Alexandria, Virginia 22314	20
Dr. James Probus Office of the Assistant Secretary of the Navy (R&D) Room 4E741, The Pentagon Washington, D. C. 20350	1
Mr. Allan D. Simon Office of the Secretary of Defense DDR&E Room 3E1040, The Pentagon Washington, D. C. 20301	1
CAPT J. Kelly Naval Electronics Systems Command Code EPO-3 Washington, D. C. 20360	1
Chief of Naval Operations Room 5B718, The Pentagon Washington, D. C. 20350 Attn: Mr. Benjamin Rosenberg	1
Chief of Naval Operations Rm 4C559, The Pentagon Washington, D. C. 20350 Attn: DCR J. M. Van Metre	1
Chief of Naval Operations 801 No. Randolph St. Arlington, Virginia 22203	1
Dr. Melvin J. Jacobson Rensselaer Polytechnic Institute Troy, New York 12181	1
Dr. Charles Stutt General Electric Co. P. O. Box 1088 Schenectady, New York 12301	1

DISTRIBUTION LIST (Cont.)

	No. of Copies
Dr. Alan Winder EDO Corporation College Point, New York 11356	1
Dr. T. G. Birdsall Cooley Electronics Lab. University of Michigan Ann Arbor, Michigan 48105	1
Dr. John Steinberg University of Miami Institute of Marine & Atmospheric Sciences Miami, Florida 33149	1
Mr. Robert Cunningham Bendix Corporation 11600 Sherman Way North Hollywood, California 91606	1
Dr. H. S. Hayre University of Houston Cullen Boulevard Houston, Texas 77004	1
Dr. Robert R. Brockhurst Woods Hole Oceanographic Institute Woods Hole, Massachusetts 02543	1
Dr. Stephen Wolff Johns Hopkins University Baltimore, Maryland 21218	1
Dr. M. A. Basin Litton Industries 8000 Woodley Avenue Van Nuys, California 91409	1
Dr. Albert Nuttall Navy Underwater Systems Center Fort Trumbull New London, Connecticut 06320	1

DISTRIBUTION LIST (Cont.)

	No. of Copies
Dr. Philip Stocklin Raytheon Company P. O. Box 360 Newport, Rhode Island 02841	1
Dr. H. W. Marsh Navy Underwater Systems Center Fort Trumbull New London, Connecticut 06320	1
Dr. David Middleton 35 Concord Ave., Apt. #1 Cambridge, Massachusetts 02138	1
Mr. Richard Vesper Perkin-Elmer Corporation Electro-Optical Division Norwald, Connecticut 06852	1
Dr. Donald W. Tufts University of Rhode Island Kingston, Rhode Island 02881	1
Dr. Loren W. Nolte Dept. of Electrical Engineering Duke University Durham, North Carolina 27706	1
Mr. S. W. Autrey Hughes Aircraft Co. P. O. Box 3310 Fullerton, California 92634	1
Dr. Thomas W. Ellis Texas Instruments, Inc. 13500 North Central Expressway Dallas, Texas 75231	1
Mr. Robert Swarts Honeywell, Inc. Marine Systems Center 5303 Shilshole Ave., N.W. Seattle, Washington 98107	1

DISTRIBUTION LIST (Cont.)

	No. of Copies
Mr. Gordon R. Hamilton Palisades Geophysical Sofar Station APO New York 09856	1
Mr. Charles Loda Institute for Defense Analyses 400 Army-Navy Drive Arlington, Virginia 22202	1
Mr. Beaumont Buck General Motors Corporation Defense Research Division 6767 Holister Ave. Goleta, California 93017	1
Dr. M. Weinstein Underwater Systems, Inc. 8121 Georgia Avenue Silver Spring, Maryland 20910	1
Dr. Harold Saxton 1601 Research Blvd. TRACOR, Inc. Rockville, Maryland 20850	1
Dr. Thomas G. Kincaid General Electric Company P. O. Box 1088 Schenectady, New York	1
Applied Research Laboratories The University of Texas at Austin Austin, Texas 78712 Attn: Dr. Loyd Hampton Dr. Charles Wood	3
Dr. Paul McElroy Woods Hole Oceanographic Institution Woods Hole, Massachusetts 02543	1

DISTRIBUTION LIST (Cont.)

	No. of Copies
Dr. John Bouyoucos General Dynamics/Electronics 1400 N. Goodman Street P. O. Box 226 Rochester, New York 14603	1
Hydrospace Research Corporation 5541 Nicholson Lane Rockville, Maryland 20852 Attn: CDR Craig Olson	1
Cooley Electronics Laboratory University of Michigan Ann Arbor, Michigan 48105	25